2014

Quantitative evaluation of atlas-based highdensity diffuse optical tomography for imaging of the human visual cortex

Xue Wu
University of Birmingham
Adam T. Eggebrecht
Washington University School of Medicine in St. Louis
Silvina L. Ferradal
Washington University School of Medicine in St. Louis
Joseph P. Culver
Washington University School of Medicine in St. Louis
Hamid Dehghani
Washington University School of Medicine in St. Louis

Biomedical Optics EXPRESS

Quantitative evaluation of atlas-based high-density diffuse optical tomography for imaging of the human visual cortex

Xue Wu,[1,*] Adam T. Eggebrecht,[2] Silvina L Ferradal,[2,3] Joseph P. Culver,[2,3] and Hamid Dehghani[1]

[1.] *School of Computer Science, University of Birmingham, Birmingham, B15 2TT, UK*
[2.] *Department of Radiology, Washington University School of Medicine, 4525 Scott Avenue, St Louis, MO, 63110, USA*
[3.] *Department of Biomedical Engineering, Washington University, One Brookings Drive, St. Louis, MO, 63130, USA*
** X.Wu.3@cs.bham.ac.uk*

Abstract: Image recovery in diffuse optical tomography (DOT) of the human brain often relies on accurate models of light propagation within the head. In the absence of subject specific models for image reconstruction, the use of atlas based models are showing strong promise. Although there exists some understanding in the use of some limited rigid model registrations in DOT, there has been a lack of a detailed analysis between errors in geometrical accuracy, light propagation in tissue and subsequent errors in dynamic imaging of recovered focal activations in the brain. In this work 11 different rigid registration algorithms, across 24 simulated subjects, are evaluated for DOT studies in the visual cortex. Although there exists a strong correlation (R^2 = 0.97) between geometrical surface error and internal light propagation errors, the overall variation is minimal when analysing recovered focal activations in the visual cortex. While a subject specific mesh gives the best results with a 1.2 mm average location error, no single algorithm provides errors greater than 4.5 mm. This work demonstrates that the use of rigid algorithms for atlas based imaging is a promising route when subject specific models are not available.

OCIS codes: (110.6960) Tomography; (170.2655) Functional monitoring and imaging; (170.3010) Image reconstruction techniques; (170.3660) Light propagation in tissues.

References and links

1. T. O. McBride, B. W. Pogue, S. Poplack, S. Soho, W. A. Wells, S. Jiang, U. L. Osterberg, and K. D. Paulsen, "Multispectral near-infrared tomography: a case study in compensating for water and lipid content in hemoglobin imaging of the breast," J. Biomed. Opt. **7**(1), 72–79 (2002).
2. J. P. Culver, T. Durduran, D. Furuya, C. Cheung, J. H. Greenberg, and A. G. Yodh, "Diffuse optical tomography of cerebral blood flow, oxygenation, and metabolism in rat during focal ischemia," J. Cereb. Blood Flow Metab. **23**(8), 911–924 (2003).
3. J. P. Culver, R. Choe, M. J. Holboke, L. Zubkov, T. Durduran, A. Slemp, V. Ntziachristos, B. Chance, and A. G. Yodh, "Three-dimensional diffuse optical tomography in the parallel plane transmission geometry: evaluation of a hybrid frequency domain/continuous wave clinical system for breast imaging," Med. Phys. **30**(2), 235–247 (2003).
4. B. R. White, A. Z. Snyder, A. L. Cohen, S. E. Petersen, M. E. Raichle, B. L. Schlaggar, and J. P. Culver, "Resting-state functional connectivity in the human brain revealed with diffuse optical tomography," Neuroimage **47**(1), 148–156 (2009).
5. B. W. Zeff, B. R. White, H. Dehghani, B. L. Schlaggar, and J. P. Culver, "Retinotopic mapping of adult human visual cortex with high-density diffuse optical tomography," Proc. Natl. Acad. Sci. U.S.A. **104**(29), 12169–12174 (2007).
6. D. A. Boas, A. M. Dale, and M. A. Franceschini, "Diffuse optical imaging of brain activation: approaches to optimizing image sensitivity, resolution, and accuracy," Neuroimage **23**(Suppl 1), S275–S288 (2004).

#214009 - $15.00 USD Received 13 Jun 2014; revised 21 Aug 2014; accepted 25 Sep 2014; published 13 Oct 2014

7. T. Austin, A. P. Gibson, G. Branco, R. M. Yusof, S. R. Arridge, J. H. Meek, J. S. Wyatt, D. T. Delpy, and J. C. Hebden, "Three dimensional optical imaging of blood volume and oxygenation in the neonatal brain," Neuroimage **31**(4), 1426–1433 (2006).
8. E. Gratton, S. Fantini, M. A. Franceschini, G. Gratton, and M. Fabiani, "Measurements of scattering and absorption changes in muscle and brain," Philos. Trans. R. Soc. Lond. B Biol. Sci. **352**(1354), 727–735 (1997).
9. S. M. Liao, S. L. Ferradal, B. R. White, N. Gregg, T. E. Inder, and J. P. Culver, "High-density diffuse optical tomography of term infant visual cortex in the nursery," J. Biomed. Opt. **17**(8), 081414 (2012).
10. D. K. Joseph, T. J. Huppert, M. A. Franceschini, and D. A. Boas, "Diffuse optical tomography system to image brain activation with improved spatial resolution and validation with functional magnetic resonance imaging," Appl. Opt. **45**(31), 8142–8151 (2006).
11. S. R. Hintz, D. A. Benaron, A. M. Siegel, A. Zourabian, D. K. Stevenson, and D. A. Boas, "Bedside functional imaging of the premature infant brain during passive motor activation," J. Perinat. Med. **29**(4), 335–343 (2001).
12. C. G. Favilla, R. C. Mesquita, M. Mullen, T. Durduran, X. Lu, M. N. Kim, D. L. Minkoff, S. E. Kasner, J. H. Greenberg, A. G. Yodh, and J. A. Detre, "Optical bedside monitoring of cerebral blood flow in acute ischemic stroke patients during head-of-bed manipulation," Stroke **45**(5), 1269–1274 (2014).
13. B. R. White and J. P. Culver, "Quantitative evaluation of high-density diffuse optical tomography: *in vivo* resolution and mapping performance," J. Biomed. Opt. **15**(2), 026006 (2010).
14. C. Habermehl, S. Holtze, J. Steinbrink, S. P. Koch, H. Obrig, J. Mehnert, and C. H. Schmitz, "Somatosensory activation of two fingers can be discriminated with ultrahigh-density diffuse optical tomography," Neuroimage **59**(4), 3201–3211 (2012).
15. S. P. Koch, C. Habermehl, J. Mehnert, C. H. Schmitz, S. Holtze, A. Villringer, J. Steinbrink, and H. Obrig, "High-resolution optical functional mapping of the human somatosensory cortex," Front Neuroenergetics **2**, 12 (2010).
16. A. T. Eggebrecht, S. L. Ferradal, A. Robichaux-Viehoever, M. S. Hassanpour, H. Dehghani, A. Z. Snyder, T. Hershey, and J. P. Culver, "Mapping distributed brain function and networks with diffuse optical tomography," Nat. Photonics **8**(6), 448–454 (2014).
17. F. H. Tian, H. J. Niu, B. Khan, G. Alexandrakis, K. Behbehani, and H. L. Liu, "Enhanced Functional Brain Imaging by Using Adaptive Filtering and a Depth Compensation Algorithm in Diffuse Optical Tomography," IEEE Trans. Med. Imaging **30**(6), 1239–1251 (2011).
18. A. T. Eggebrecht, B. R. White, S. L. Ferradal, C. Chen, Y. Zhan, A. Z. Snyder, H. Dehghani, and J. P. Culver, "A quantitative spatial comparison of high-density diffuse optical tomography and fMRI cortical mapping," Neuroimage **61**(4), 1120–1128 (2012).
19. D. A. Boas and A. M. Dale, "Simulation study of magnetic resonance imaging-guided cortically constrained diffuse optical tomography of human brain function," Appl. Opt. **44**(10), 1957–1968 (2005).
20. A. Custo, D. A. Boas, D. Tsuzuki, I. Dan, R. Mesquita, B. Fischl, W. E. Grimson, and W. Wells 3rd, "Anatomical atlas-guided diffuse optical tomography of brain activation," Neuroimage **49**(1), 561–567 (2010).
21. S. L. Ferradal, A. T. Eggebrecht, M. Hassanpour, A. Z. Snyder, and J. P. Culver, "Atlas-based head modeling and spatial normalization for high-density diffuse optical tomography: in vivo validation against fMRI," Neuroimage **85**(Pt 1), 117–126 (2014).
22. R. J. Cooper, M. Caffini, J. Dubb, Q. Fang, A. Custo, D. Tsuzuki, B. Fischl, W. Wells 3rd, I. Dan, and D. A. Boas, "Validating atlas-guided DOT: a comparison of diffuse optical tomography informed by atlas and subject-specific anatomies," Neuroimage **62**(3), 1999–2006 (2012).
23. J. Mazziotta, A. Toga, A. Evans, P. Fox, J. Lancaster, K. Zilles, R. Woods, T. Paus, G. Simpson, B. Pike, C. Holmes, L. Collins, P. Thompson, D. MacDonald, M. Iacoboni, T. Schormann, K. Amunts, N. Palomero-Gallagher, S. Geyer, L. Parsons, K. Narr, N. Kabani, G. Le Goualher, J. Feidler, K. Smith, D. Boomsma, H. Hulshoff Pol, T. Cannon, R. Kawashima, and B. Mazoyer, "A four-dimensional probabilistic atlas of the human brain," J. Am. Med. Inform. Assoc. **8**(5), 401–430 (2001).
24. J. Mazziotta, A. Toga, A. Evans, P. Fox, J. Lancaster, K. Zilles, R. Woods, T. Paus, G. Simpson, B. Pike, C. Holmes, L. Collins, P. Thompson, D. MacDonald, M. Iacoboni, T. Schormann, K. Amunts, N. Palomero-Gallagher, S. Geyer, L. Parsons, K. Narr, N. Kabani, G. Le Goualher, D. Boomsma, T. Cannon, R. Kawashima, and B. Mazoyer, "A probabilistic atlas and reference system for the human brain: International Consortium for Brain Mapping (ICBM)," Philos. Trans. R. Soc. Lond. B Biol. Sci. **356**(1412), 1293–1322 (2001).
25. J. West, J. M. Fitzpatrick, M. Y. Wang, B. M. Dawant, C. R. Maurer, Jr., R. M. Kessler, and R. J. Maciunas, "Retrospective intermodality registration techniques for images of the head: surface-based versus volume-based," IEEE Trans. Med. Imaging **18**(2), 144–150 (1999).
26. J. B. West, J. M. Fitzpatrick, S. A. Toms, C. R. Maurer, Jr., and R. J. Maciunas, "Fiducial point placement and the accuracy of point-based, rigid body registration," Neurosurgery **48**(4), 810–816 (2001).
27. C. R. Maurer, Jr., J. M. Fitzpatrick, M. Y. Wang, R. L. Galloway, Jr., R. J. Maciunas, and G. S. Allen, "Registration of Head Volume Images Using Implantable Fiducial Markers," IEEE Trans. Med. Imaging **16**(4), 447–462 (1997).
28. H. J. Huppertz, M. Otte, C. Grimm, R. Kristeva-Feige, T. Mergner, and C. H. Lücking, "Estimation of the accuracy of a surface matching technique for registration of EEG and MRI data," Electroencephalogr. Clin. Neurophysiol. **106**(5), 409–415 (1998).
29. A. K. Singh, M. Okamoto, H. Dan, V. Jurcak, and I. Dan, "Spatial registration of multichannel multi-subject fNIRS data to MNI space without MRI," Neuroimage **27**(4), 842–851 (2005).

#214009 - $15.00 USD Received 13 Jun 2014; revised 21 Aug 2014; accepted 25 Sep 2014; published 13 Oct 2014

30. W. R. Crum, T. Hartkens, and D. L. G. Hill, "Non-rigid image registration: theory and practice," Br. J. Radiol. **77**(2), S140–S153 (2004).
31. B. A. Ardekani, S. Guckemus, A. Bachman, M. J. Hoptman, M. Wojtaszek, and J. Nierenberg, "Quantitative comparison of algorithms for inter-subject registration of 3D volumetric brain MRI scans," J. Neurosci. Methods **142**(1), 67–76 (2005).
32. A. Klein, J. Andersson, B. A. Ardekani, J. Ashburner, B. Avants, M. C. Chiang, G. E. Christensen, D. L. Collins, J. Gee, P. Hellier, J. H. Song, M. Jenkinson, C. Lepage, D. Rueckert, P. Thompson, T. Vercauteren, R. P. Woods, J. J. Mann, and R. V. Parsey, "Evaluation of 14 nonlinear deformation algorithms applied to human brain MRI registration," Neuroimage **46**(3), 786–802 (2009).
33. M. Jermyn, H. Ghadyani, M. A. Mastanduno, W. Turner, S. C. Davis, H. Dehghani, and B. W. Pogue, "Fast segmentation and high-quality three-dimensional volume mesh creation from medical images for diffuse optical tomography," J. Biomed. Opt. **18**(8), 086007 (2013).
34. H. Dehghani, M. E. Eames, P. K. Yalavarthy, S. C. Davis, S. Srinivasan, C. M. Carpenter, B. W. Pogue, and K. D. Paulsen, "Near infrared optical tomography using NIRFAST: Algorithm for numerical model and image reconstruction," Commun. Numer. Methods Eng. **25**(6), 711–732 (2009).
35. J. Ashburner and K. J. Friston, "Image segmentation," in *Human Brain Function,* 2nd ed., R. S. J. Frackowiak, K. J. Friston, C. Frith, R. Dolan, C. J. Price, S. Zeki, J. Ashburner, and W. D. Penny, eds. (Academic Press, 2003).
36. K. J. Friston, "Introduction: experimental design and statistical parametric mapping," in *Human brain function,* 2nd ed., R. S. J. Frackowiak, K. J. Friston, C. Frith, R. Dolan, C. J. Price, S. Zeki, J. Ashburner, and W. D. Penny, eds. (Academic Press, 2003).
37. F. Bevilacqua, D. Piguet, P. Marquet, J. D. Gross, B. J. Tromberg, and C. Depeursinge, "In vivo local determination of tissue optical properties: applications to human brain," Appl. Opt. **38**(22), 4939–4950 (1999).
38. A. Bluestone, G. Abdoulaev, C. Schmitz, R. Barbour, and A. Hielscher, "Three-dimensional optical tomography of hemodynamics in the human head," Opt. Express **9**(6), 272–286 (2001).
39. D. A. Boas, T. Gaudette, G. Strangman, X. Cheng, J. J. Marota, and J. B. Mandeville, "The accuracy of near infrared spectroscopy and imaging during focal changes in cerebral hemodynamics," Neuroimage **13**(1), 76–90 (2001).
40. D. Chetverikov, D. Svirko, D. Stepanov, and P. Krsek, "The trimmed iterative closest point algorithm," Int. C Patt. Recog. **3**, 545–548 (2002).
41. U. Herwig, P. Satrapi, and C. Schönfeldt-Lecuona, "Using the International 10-20 EEG system for positioning of transcranial magnetic stimulation," Brain Topogr. **16**(2), 95–99 (2003).
42. P. Giacometti, K. L. Perdue, and S. G. Diamond, "Algorithm to find high density EEG scalp coordinates and analysis of their correspondence to structural and functional regions of the brain," J. Neurosci. Methods **229**, 84–96 (2014).
43. V. Jurcak, D. Tsuzuki, and I. Dan, "10/20, 10/10, and 10/5 systems revisited: their validity as relative head-surface-based positioning systems," Neuroimage **34**(4), 1600–1611 (2007).
44. Y. Zhan, A. T. Eggebrecht, J. P. Culver, and H. Dehghani, "Image quality analysis of high-density diffuse optical tomography incorporating a subject-specific head model," Front. Neuroenergetics **4**, 6 (2012).
45. T. Durduran, G. Yu, M. G. Burnett, J. A. Detre, J. H. Greenberg, J. Wang, C. Zhou, and A. G. Yodh, "Diffuse optical measurement of blood flow, blood oxygenation, and metabolism in a human brain during sensorimotor cortex activation," Opt. Lett. **29**(15), 1766–1768 (2004).
46. H. Dehghani, B. R. White, B. W. Zeff, A. Tizzard, and J. P. Culver, "Depth sensitivity and image reconstruction analysis of dense imaging arrays for mapping brain function with diffuse optical tomography," Appl. Opt. **48**(10), D137–D143 (2009).
47. Y. Pei, H. L. Graber, and R. L. Barbour, "Influence of Systematic Errors in Reference States on Image Quality and on Stability of Derived Information for dc Optical Imaging," Appl. Opt. **40**(31), 5755–5769 (2001).
48. G. Strangman, M. A. Franceschini, and D. A. Boas, "Factors affecting the accuracy of near-infrared spectroscopy concentration calculations for focal changes in oxygenation parameters," Neuroimage **18**(4), 865–879 (2003).

1. Introduction

Diffuse optical tomography (DOT), also known as near infrared tomography is a functional imaging modality for soft biological tissue [1]. DOT is capable of measuring the intrinsic absorption and scattering in diffuse media using Near Infrared (NIR) light (wavelengths between 650 and 1000 nm), which are then used to derive spatially resolved maps of tissue chromophore concentrations such as oxygenated and deoxygenated haemoglobin. DOT has been applied to monitor tissue metabolic state [2], breast cancer diagnosis [3], imaging functional activity in the human brain [4–6] and neonatal brain monitoring [7–9]. While most hemodynamic-based neuroimaging research studies in adult subjects are typically performed using functional magnetic resonance imaging (fMRI), its relative high cost, fixed scanner

#214009 - $15.00 USD Received 13 Jun 2014; revised 21 Aug 2014; accepted 25 Sep 2014; published 13 Oct 2014

locations and physical constraints during imaging, limit fMRI's translation as a bedside clinical tool [10]. DOT has shown a strong potential in clinical application specifically for neonate and long-term bedridden patients [11] and NIR studies of the human brain have demonstrated its ability to recover abnormalities as haemorrhage detection from stroke patients [12] with accurate recovery of stimulated activations [13–15] and functional networks [5, 16, 17].

In the recovery process of brain activations using DOT, a forward model is used for the simulation of NIR light propagation within the head. An inverse process based on this forward model is then used to recover the changes in the optical properties associated with functional activations. It is therefore imperative that the forward model accurately represents the subject being imaged as the propagation of light within tissue is a non-linear function of both shape, size and internal structure and (often assumed) underlying optical properties. Where available, the forward model is based on a subject-specific anatomical head model: structural MRI provides a-priori information about the absolute geometry and internal structures of the head [18, 19]. When subject specific models are not available, a registered (atlas based) anatomical head model can be used as an alternative [20–22]. The head atlas often used is a model that contains the structural information of the human brain based on an average of multiple subjects. For example the ICBM152 atlas as generated in the ICBM project uses segmented and co-registered MRI images from 152 subjects and is widely used [23, 24]. An atlas such as this can be used to provide internal structural information as well as an approximation of the external head shape instead of subject-specific MRI in atlas-based DOT.

Registration between the atlas and the subject being imaged using DOT is one of the main steps in atlas-based DOT of the human brain and therefore the evaluation of the accuracy of the registration methods themselves has been of great importance. Different registration methods can be used based on either rigid or non-rigid methods as well as different number of registration points (also referred to as landmark or fiducial markers) from the external surface or volumes [25, 26]. The utilisation of registration methods within human brain imaging has been used for either registering different types of images such as CT and MRI from same subject or registering image data from different subjects into an atlas space (for data analysis) [27], while its use in DOT is relatively new but has received much attention [20, 21].

A surface based rigid registration method has been utilised by Huppertz et al [28] for EEG and MRI data by matching the surface from a 3D scanning device to the surface extracted from MRI images. Using this method the average error was found to be 0.3 mm based on the location error of fiducial points of the head surface, namely, the location of electrodes in EEG system. The size and distribution of fiducial points used for registration is also an important aspect which was investigated by West et al. which focused on fiducial point-based registration for cranial neurosurgery [26]. This study showed that the landmarks must be narrower than 4 mm to get a registration with an acceptable error while increasing the number of fiducial points and avoiding near-collinear configurations also improved the registration accuracy. Singh et al developed a fiducial point-based registration method that registered multichannel, multi-subject NIR data to MNI space (a standard atlas space developed at the Montreal Neurological Institute) which used 19 fiducial points from EEG 10/20 landmark system and an iterative closest point algorithm for the optimization [29]. The accuracy of the method was evaluated by the closest surface points on the registered model and the atlas with the location error found to be within 4.7 to 7.0 mm.

Non-rigid registration is most commonly used in studies where subject-specific data needs to be registered with an average model or reference space such as MNI space for analysis. Different combinations of this approach can be used. For example, Crum et al. divided the non-rigid registration into geometric approaches (registration methods based on anatomical information) and intensity approaches (registration methods based on intensity

#214009 - $15.00 USD Received 13 Jun 2014; revised 21 Aug 2014; accepted 25 Sep 2014; published 13 Oct 2014

patterns) which demonstrated that combining geometric and intensity approaches is a more robust method for registration of human brain image [30]. There are a number of different toolboxes available publicly to allow non-rigid deformation and three of these were compared by Ardekania et al. using brain MRI scans [31]. The algorithms compared were the Automatic Image Registration (AIR; version 5), the Statistical Parametric Mapping (SPM99), and the Automatic Registration Toolbox packages (ART). These comparisons showed that all algorithms provide accuracy within geometrical error of less than 2.0 mm. Klein et al. focused on the evaluation and comparison between 14 non-rigid and 1 rigid registration method based on calculated overlay between different brain regions from an average head and registered subject models from different subjects [32]. It was shown that non-rigid registration is more accurate providing an average accuracy of 75% in overlay. However, non-rigid methods often require both surface information and the internal structure of the subject head, while rigid methods can be used when the internal information is not available, which is a common problem faced with atlas based image recovery in DOT.

Previous studies in utilisation of atlas based DOT are focused on evaluation of the accuracy in reconstruction result directly. In these studies, the accuracy of the recovered images are evaluated by comparison between a reference and the atlas-based reconstruction with the evaluation criteria typically generated mostly based on the localization error or overlapping percentage of the two reconstructed areas. Custo et al. compared the DOT recovery of the same brain activation based on subject-specific models and the corresponding registered atlas [20]. The atlas was registered to each individual subject based on a rigid registration using fiducial points from EEG 10/20 system. 3 subjects were used in the study and the results from the subject and the registered atlas based model showed ~70% overlay. Cooper et al. also focused on comparison of DOT recovery using subject-specific and registered models using the same registration method as Custo et al. but using simulated data from 32 subjects [22]. The accuracy of the recovery result was evaluated based on mean Euclidean, mean geodesic and mean Hausdorff error. Localization error of atlas based DOT was approximately 18 mm in Euclidean space, and 9 mm for DOT with subject-specific model. Based on this study although the atlas based DOT demonstrated larger reconstruction errors, it was deemed as an acceptable alternative when subject-specific model is not available. Ferradal et al. used a similar landmark system after adjusting the fiducial location that concentrate on the region of interest being imaged (visual cortex) [21]. Subject specific and atlas based DOT with linear registration and a non-linear registration method based on a B-spline transformation were compared to fMRI data for comparisons using a group analysis. For the group analysis, each subject was registered to the standard atlas and the reconstructed activation was generated based on statistical tests. Atlas-based DOT had an average localization error of 2.7mm compared to subject-specific model, and 6.6mm to fMRI. Although all of these studies are focused on evaluation of the recovered activations (images) from a ‘single’ registration method, they show that in their respective studies, the reconstructions based on an atlas model have acceptable accuracy using both simulated and experimental data and can be considered as an alternative when subject specific anatomical mesh is not available.

The previous works in atlas based DOT discussed above are focused on investigation and comparison of the registration method based on a ‘single’ fiducial points system in terms of geometrical error and/or the recovered activation. To date, the effect of registration algorithm or fiducial number and location on atlas-based DOT data quality have yet to be fully evaluated. As model-based image recovery in DOT relies on accurate models for light propagation, no work to date has investigated the effect of registration errors on consequent errors in the light model, which directly affects the parameter recovery accuracy. The optical properties of the human head can be modeled with 5 major layers, skin, scalp, bone, CSF, gray matter and white matter. In ‘rigid’ registration methods that rely only on external markers these layers are also rigidly transformed. It is therefore important to not only

#214009 - $15.00 USD Received 13 Jun 2014; revised 21 Aug 2014; accepted 25 Sep 2014; published 13 Oct 2014

consider the external geometry error, but also the consequent error on the light model within the layered tissues. In summary, atlas-based DOT can be divided into three steps: 1) registration between the atlas model and the subject, 2) generation of the light propagation model using the registered atlas, and 3) recovery of brain activations. All three steps are evaluated in the presented work.

Full-head anatomical 3D images from 24 subjects are used to evaluate the accuracy of 4 different rigid registration methods, each using a combination of 5 different fiducial points, giving rise to 11 different algorithms. The accuracy of each algorithm is investigated by evaluating the error of the light propagation model thereby considering the quality of not just the external registration, but also the effects of registration of the internal structures. Finally to demonstrate the overall consequence on parameter recovery, each of the 11 algorithms are evaluated using simulated functional activation data from the visual cortex for all 24 subjects.

2. Methods

Image recovery in DOT using measured NIR data from a human subject involves data calibration (data-preprocessing) as well as model based image reconstruction. Data calibration is a critical aspect of image reconstruction regardless of the modeling method utilized and is covered in detail elsewhere [5]. Regardless of whether using subject specific or atlas-based models, the domain of interest needs to be segmented and meshed, which is achieved using NIRVIEW [33]. For model based image reconstruction, different models of light propagation in tissue can be utilized; in this work we use a finite element model (FEM) of the head using the open source package NIRFAST [34].

2.1 Subject specific models

Image recovery using subject specific models can be summarized using the flowchart shown in Fig. 1. Specifically, MRI data from a given subject is used together with Statistical Parametric Mapping (SPM) [35, 36] which first allows a parametric segmentation of the 5 tissue types (skin, bone, CSF, gray and white matter) based on the pixel intensity probability function distribution, which is then used together with NIRVIEW and NIRFAST to create masks and layered volumetric FEM meshes. The optical properties used for each layer are typically accepted to be subject specific, but throughout this work, the values shown in Table 1 are used [37–39].

Table 1. Head tissue optical properties at 750 nm

	μ_a (mm^{-1}) / μ'_s (mm^{-1})
Scalp	0.0170 / 0.74
Skull	0.0116 / 0.94
CSF	0.004 / 0.3
Gray Matter	0.0180 / 0.8359
White Matter	0.0167 / 1.1908

#214009 - $15.00 USD Received 13 Jun 2014; revised 21 Aug 2014; accepted 25 Sep 2014; published 13 Oct 2014

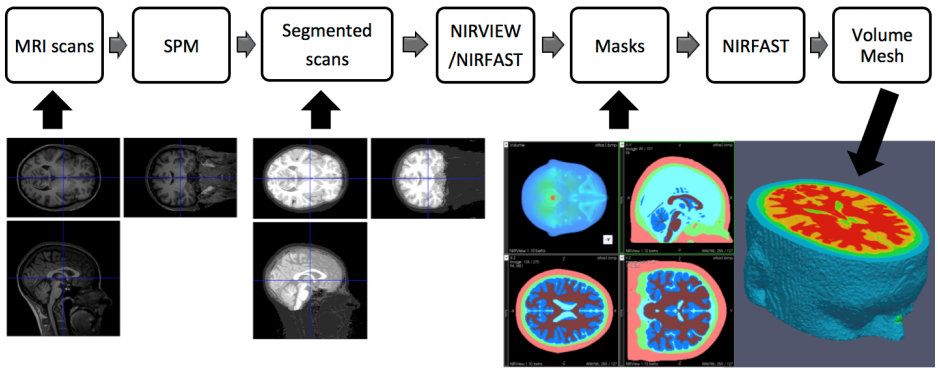

Fig. 1. Workflow of creating subject specific models from subject MRI.

2.2 Atlas based models

Registration for DOT recovery using atlas based models can be summarized using the flowchart in Fig. 2. Specifically, for atlas based DOT there are 3 major steps: 1) Registration of the atlas: affine transformation matrices are generated based on fiducial points extracted from surfaces of the atlas model and the subject head. These transformation matrices are then applied to the atlas model to generate the registered atlas based light model in the subject specific space. All transformed FEM models are then checked for consistency and accuracy using NIRFAST [32]. 2) Generation of the forward model where NIR light propagation through the domain is simulated based on the registered atlas model. The internal structures of the head are provided by registered atlas, based entirely on registration of the external surface. 3) Recovering the activation maps: The model of light from step 2 is used to calculate the sensitivity matrix which is then used to calculate the optical property changes based on simulated (or measured) subject specific data.

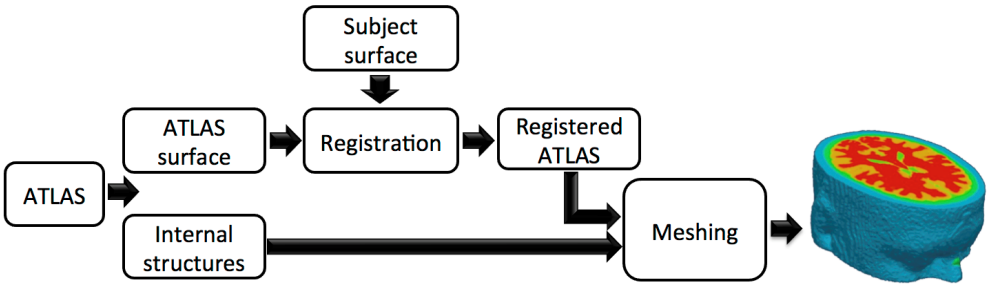

Fig. 2. Workflow of creating atlas based models using registration methods.

2.2.1 Registration methods

Landmark-based registration is a common rigid registration method for the human head. It can be used to generate an affine transformation matrix for the atlas model based on specific fiducial points as extracted from the atlas and subject head. There are two major steps in the registration process: 1) Fiducial points are extracted separately from surfaces of the atlas and subject head based on the same landmark system. 2) An affine transformation matrix is then generated and optimized by minimizing the distance between these two sets of landmarks. In order to provide a comprehensive comparison, 11 different rigid registration methods are studied and applied for the atlas based model for 24 subjects as summarized in Table 2 and Fig. 3.

#214009 - $15.00 USD Received 13 Jun 2014; revised 21 Aug 2014; accepted 25 Sep 2014; published 13 Oct 2014

Table 2. Rigid registration methods as well as different types of landmark systems used.

Method	Basic 4	EEG 19	EEG 40	Full head	Line fitting
ICP		✖	✖	✖	
IP2P		✖	✖	✖	
NP2P	✖	✖	✖	✖	
Line fitting					✖

2.2.2 Optimisation algorithms

The second step of the registration consists of the generation of the affine transformation matrix that is optimized based on an algorithm which minimizes the distance between landmark pairs from subject and atlas models. Three algorithms are used in this study: 1) iterative Point to Point algorithm (P2P), 2) Non-iterative Point to Point algorithm (NP2P), and 3) Iterative Closest Point algorithm (ICP).

In the P2P optimisation algorithm, there is a one-to-one corresponding relationship between landmarks from the subject and atlas model since the two landmarks sets are extracted based on the same landmark system. The P2P algorithm pairs corresponding landmarks from the subject and the atlas, and optimises the affine transformation matrix by minimizing the distance between the set of corresponding landmark pairs. The optimisation progresses iteratively through two steps:

1. Generation of an affine transformation matrix based on minimisation of the mean square error (MSE) between the paired landmarks [Eq. (1)]:

$$T = arg_T min \sum_{i=1}^{n} \left\| T * Atlas_i - Sub_i \right\| \tag{1}$$

where T is the affine transformation matrix, n is number of pairs in the landmark system, $Atlas_i$ is a landmark from atlas model and Sub_i is the corresponding landmark of $Atlas_i$ from subject i.

2. Generation of the registered atlas model by applying the affine transformation matrix to the atlas and as well as the landmarks set [Eq. (2)]:

$$Atlas_i^k = T_k Atlas_i^{k-1} \tag{2}$$

where $Atlas_i^k$ is the landmark from subject surface from iteration k and T_k is the corresponding affine transformation matrix. The registered model is then used as the atlas model in the next iteration. These processes are then repeated until the difference between iterative changes in the mean squared error is below some threshold.

The NP2P optimisation algorithm is similar to P2P except the two steps of optimisation are only processed once. Compared to the iterative process, the Non-iterative process has a shorter processing time.

The ICP optimisation algorithm is also similar to P2P except that a different pairing function is utilised [40]. Specifically, in the ICP algorithm the landmarks from the atlas model are paired with their closest landmarks from the subject, and the landmark pairs are reselected after each iteration based on their closest pairs.

#214009 - $15.00 USD Received 13 Jun 2014; revised 21 Aug 2014; accepted 25 Sep 2014; published 13 Oct 2014

2.2.3 Landmark systems

Four different landmark systems are investigated in this study. The first landmark system is basic-4 landmark system, Fig. 3(a), which contains landmarks from four anatomically specified points: the nasion, which is the depressed area between the eyes and above the bridge of the nose; the inion, which is the most prominent point at the back of the head; and the two temples which are the area on the scalp above the ears. These four landmarks can be easily extracted manually from surface of heads. Since there are only four fiducial points in this basic-4-landmark system, only the NP2P algorithm is applied to this system, as further iterations do not provide additional improvements.

Second and third landmark systems are EEG-19 and EEG-40 landmark systems Fig. 3(b) and 3(c). They both extract landmarks based on the location of scalp electrodes as defined by the EEG10/20 landmark systems [41–43]. Landmarks locations in these systems are selected based on distances among adjacent landmarks as well as the distances between these and the four basic anatomical landmarks. These two landmark systems are similar except for the density of fiducial points. EEG-19 landmark system is an EEG10/20 landmark system with 19 fiducial points for each subject, and EEG-40 is an EEG10/20 landmark system with 40 fiducial points. All three optimization algorithms are applied to these two landmark systems.

The forth landmark system is a full-head landmark, Fig. 3(d), which places a high-density grid on the surface of the head based on the basic-4 landmarks and extracts landmarks uniformly from the grid, excluding facial features. This landmark system contains 700 fiducial points evenly distributed across the whole scalp covering the cerebral cortex. All three optimization algorithms are applied to this landmark system.

A line-fitting-based registration is also used, which generates and optimizes the affine transformation matrix by fitting curves extracted from the surface of the atlas model with those from the subject head surface Fig. 3(e). Three surface curves are extracted based on the basic-4 landmarks system above and an affine transformation matrix is then optimised by minimizing the differences on a set of discrete points along each of the lines, which is processed iteratively between two steps similar to that of P2P optimisation algorithm.

Based on these landmark systems and the optimization algorithm outlined above, a comprehensive set of 11 different registration methods, Table 2, are evaluated in this study.

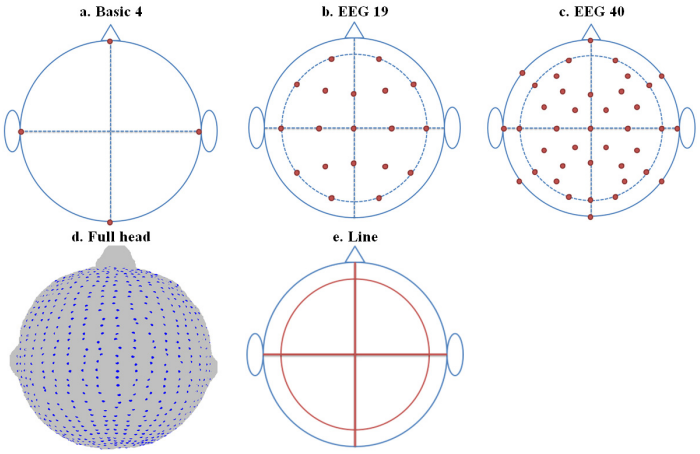

Fig. 3. Set of 5 different Landmark systems used for registration.

2.3 Geometrical error analysis

Subject specific head meshes are generated from 24 different subjects using subject specific MRIs. The atlas head mesh is generated from the ICBM152 head atlas. The atlas mesh is

#214009 - $15.00 USD Received 13 Jun 2014; revised 21 Aug 2014; accepted 25 Sep 2014; published 13 Oct 2014

then registered to each of the subject specific meshes individually using the 11 registration methods listed in Table 2. Evaluation of the geometrical error of the registered atlas model against the subject specific model is calculated with the surface distance, defined as distance from each surface node of the subject's mesh to its closest surface node of the registered atlas' mesh.

2.4 Sensitivity matrix error analysis

A high density 24 source and 28 detector pad as described elsewhere [44] is placed on the surface of the head mesh, locations of which are determined by placing centre of pads on the inion of the head, so that the whole pad is on the scalp directly above the visual cortex. The registered atlas mesh share the same location of pad centre with their correspondent subject meshes. Sensitivity matrices are then generated based on all 24 subject meshes and 264 registered atlas meshes (24 subjects × 11 registrations) using the NIRFAST software package. In the presented work, a single wavelength model based at 750 nm is considered and all the relevant optical properties for each layer within the head are given in Table 1. Relative error of the sensitivity matrices is calculated as percentage difference between sensitivity matrices generated from registered atlas models and those of the corresponding subject specific model.

2.5 Focal activation error analysis

Four individual focal activations are simulated in the four quadrants of the visual cortex for each subject. Each simulated activation has a radius of 7 mm and is limited at most to 3 mm depth from the surface of the brain (cortex). In the simulated activation region, a 24% change in optical parameter (absorption only) is set to cause at most a 5% change in the measured signal from the detectors [45]. In line with our current in vivo performance, 0.12%, 0.15%, 0.41% and 1.42% Gaussian random noise was added to first (13mm), second (30mm), third (40mm) and fourth (48mm) nearest neighbour measurements to provide realistic data [46]. Only the first to fourth nearest neighbours for each source are used for image recovery. Simulated activations are then reconstructed using the subject mesh as well as the registered atlas mesh from each of the 11 registration methods. All presented results are limited to a region of interest (ROI) defined as the region under the imaging pad to a depth of 30 mm which has been determined the maximum possible imaging depth of the visual cortex for our imaging setup [44]. For parameter recovery, a spatially-varying regularisation is used [Eq. (3), (4)].

$$\Delta\mu = \tilde{J}^T \left(\tilde{J}\tilde{J}^T + \propto I \right)^{-1} \Delta y \tag{3}$$

$$\tilde{J} = \frac{J}{\sqrt{JJ^T + \beta\left(\max\left(diag\left(JJ^T\right)\right)\right)}} \tag{4}$$

where $\propto$ is the Tikhonov regularisation parameter, β is the spatial regularisation factor, with $\propto = 0.01, \beta = 0.01$ and J is the sensitivity matrix. Δμ is the recovered change in optical properties and Δy is the change in boundary data due to the modeled focal activation. Additionally, to reduce artefacts in the reconstructions, a voxel-based Gaussian smoothing function (mean of 0 and standard deviation of 5 mm) is utilised. The recovered activation regions are then selected by thresholding the smoothed recovered changes based on either 50% or 70% of the maximum recovered changes.

The location error for the recovered activations D_c is given as Eq. (5).

$$D_c = \sqrt{(x_r - x_s)^2 + (y_r - y_s)^2 + (z_r - z_s)^2} \tag{5}$$

#214009 - $15.00 USD Received 13 Jun 2014; revised 21 Aug 2014; accepted 25 Sep 2014; published 13 Oct 2014

$$x_r = \frac{\sum_{i=1}^{nodes}(x_{ni} * \mu_{ani})}{\sum_{i=1}^{nodes}(\mu_{ani})} \tag{5.1}$$

$$y_r = \frac{\sum_{i=1}^{nodes}(y_{ni} * \mu_{ani})}{\sum_{i=1}^{nodes}(\mu_{ani})} \tag{5.2}$$

$$z_r = \frac{\sum_{i=1}^{nodes}(z_{ni} * \mu_{ani})}{\sum_{i=1}^{nodes}(\mu_{ani})} \tag{5.3}$$

where x_r y_r z_r are the coordinate of the centre of mass of the recovered activation; x_s y_s z_s are the coordinate of centre of target simulated activation; *nodes* are number of nodes in activation region; x_{ni} y_{ni} z_{ni} are the coordinate of node *i* in the region and μ_{ani} is recovered optical parameter of node *i*. The relative recovered volume of the region v_{per} is given as Eq. (6).

$$v_{per} = \frac{v_r}{v_s} * 100\% \tag{6}$$

where v_r is volume of the recovered activation; v_s is volume of the target simulated activation. The relative percentage overlay of the recovered region v_{ov} is given as Eq. (7).

$$v_{ov} = \frac{v_{overlay}}{v_s} * 100\% \tag{7}$$

where $v_{overlay}$ is volume of overlay between simulated activation and recovered activation; v_s is volume of the target simulated activation. Finally, the average contrast in the recovered activation μ_r is given as Eq. (8).

$$\mu_r = \frac{\sum_{i=1}^{nodes}(\mu_{ani}) \Big/ nodes}{\mu_{sim}} \tag{8}$$

where μ_{ani} is recovered change of optical parameter of node *i*, nodes is number of nodes in activation region. μ_{sim} is simulated change of optical parameter.

3. Results and discussions

The aim of this work is to evaluate the errors due to atlas based image reconstruction in DOT for the visual cortex. Therefore, all presented results are limited to this ROI which is directly covered by the imaging pad. To provide a qualitative example of the calculated surface distance error, results from three different registration methods for a given subject are shown in Fig. 4. Although in this example the basic-4 landmark registration has high surface distance error on the top most part of the head (>10 mm), it has the lowest surface distance within the ROI (over the visual cortex). However, although both the EEG19ICP and FullnP2P registration have higher errors over the visual cortex, they provide a better match when considering the entire head.

#214009 - $15.00 USD Received 13 Jun 2014; revised 21 Aug 2014; accepted 25 Sep 2014; published 13 Oct 2014

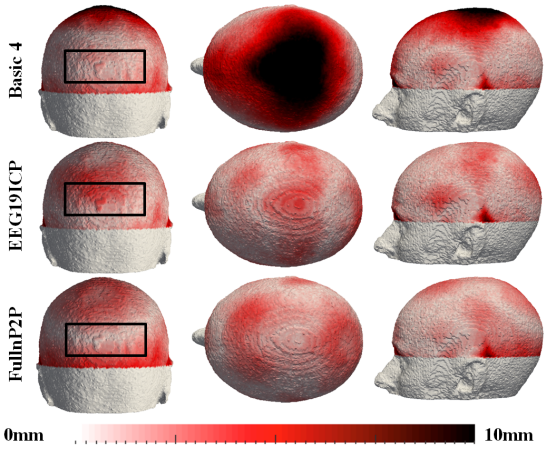

Fig. 4. Examples of calculated surface distance errors for three different registration methods. ROI is shown in black box is used for all quantitative analysis

In order to provide a more detailed analysis from different registration methods over all 24 subjects, whisker/box plots of the mean surface errors within the ROI are shown in Fig. 5. It can be seen that all registration methods have on average ~7mm surface distance error and no greater than 11 mm within the ROI. For the same landmark system, NP2P and P2P methods have a slight advantage over the ICP method. Basic-4 landmark registration, line-fitting and full-head landmark registration, with NP2P and P2P show a slight advantage over other registration methods.

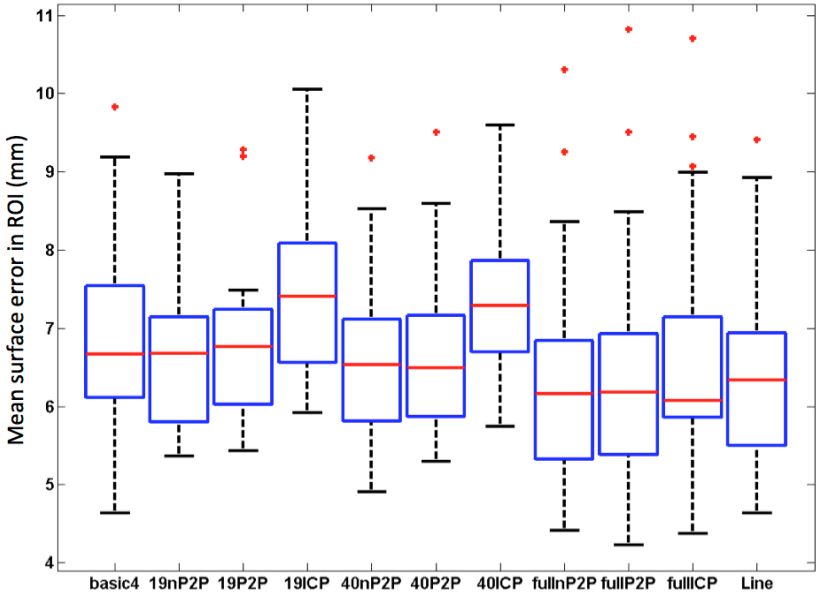

Fig. 5. Surface geometry error for different registration methods for all 24 subjects. The central (red) lines represent the median, the box plots represent the 25th and 75th percentiles, whereas the whiskers present +/– 2.7 standard deviations. Outliers are presented as red crosses.

All of the utilised registration methods rely on external landmarks for registration on to the subject model and all tissue types are deformed rigidly to provide the best match. The internal tissue structural information therefore relies only on external landmarks. Specifically

#214009 - $15.00 USD Received 13 Jun 2014; revised 21 Aug 2014; accepted 25 Sep 2014; published 13 Oct 2014

in this study, since the recovery of focal activations are expected from the cortical surface of the brain, it is necessary to evaluate the registration error not only to the external surface but also to internal structures. Figure 6 provides a qualitative example of the calculated surface distance error of the cortex from three different registration methods for a given subject. It can be seen that generally the geometric error is less than 5 mm, with the maximum error seen in the folds of the brain as expected. These errors are calculated for each registered atlas models individually, but plotted on the subject cortex.

To investigate the accuracy of registration of internal structures once registered on to the subject, it is possible to calculate the joint-histogram of the subject specific mesh against the registered mesh (Fig. 7). To achieve this, the subject specific mesh and the registered atlas mesh are interpolated to the same voxel-based grid ensuring that each node in the grid has region labels (white matter, grey matter, CSF, skull, skin and air) from the two meshes. A region difference map is then generated based on the difference between the two labels and the joint histogram is calculated. Each region is normalized based on the number of nodes in the subject specific model to allow a fair comparison and only data from the ROI is shown. It can be seen that the joint histogram of fully registered meshes (i.e. subject specific versus subject specific) provides a unit diagonal plot, indicating that all the nodes from a given region in one model matched exactly with the same nodes in another. Conversely, if two models do not match exactly, some blurring (cross-talk) between nodes of different regions will be expected. It is evident that for the example shown in Fig. 7, for all registration methods, there exists a cross-talk between air/skin tissue as well as gray/white matter. More importantly, CSF is not well registered and has a strong cross-talk with neighbouring tissue types.

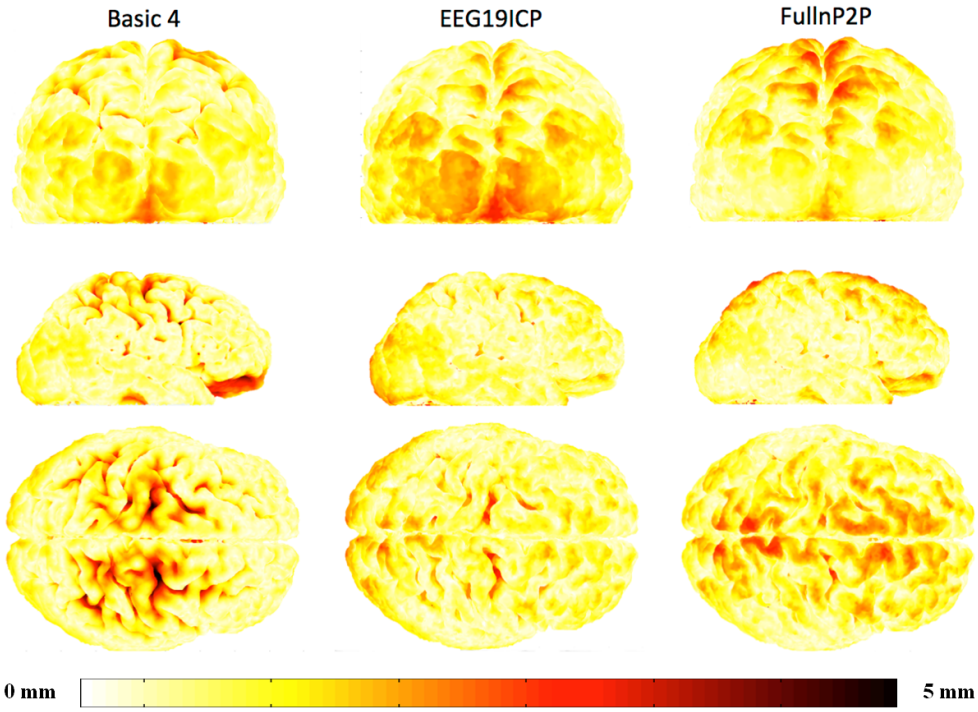

Fig. 6. Examples of calculated cortex surface errors for three different registration methods. Top row: Back view. Middle row: Side view. Bottom row: Top view.

#214009 - $15.00 USD Received 13 Jun 2014; revised 21 Aug 2014; accepted 25 Sep 2014; published 13 Oct 2014

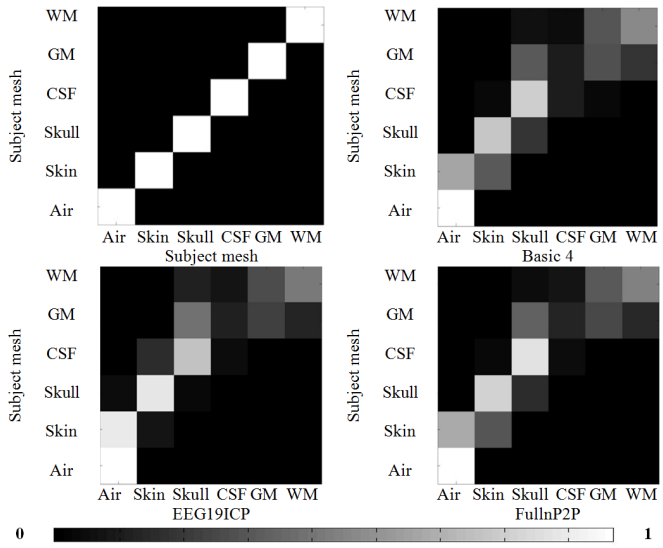

Fig. 7. Joint histograms of a single subject with different registration algorithms.

The calculation of light propagation within the head, for model based DOT, relies not only on structural information about tissue layers, but also on the accuracy of the underlying optical properties. To quantitatively demonstrate the percentage error of assumed optical properties throughout the head based on different registration methods, a spatial map of tissue absorption error is shown for a given subject in Fig. 8. This is an axial slice through the entire head, mid-way within the imaging pad. It can be see that the largest error is at the CSF/Brain interface as well as CSF/Bone. There also exists an error at the skin layer, where as expected from Fig. 7, there exists a geometric registration error on the external surface.

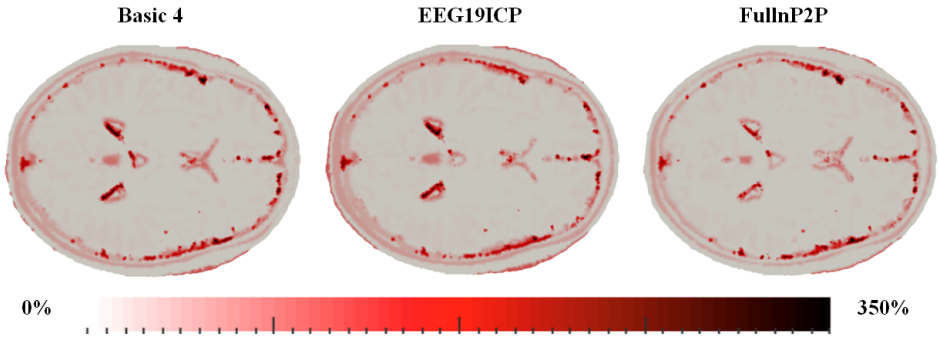

Fig. 8. Spatial map of error in tissue absorption at 750nm for a given subject for different registration methods. This is an axial slice through the registered atlas mesh, mid-way within the measurement pad.

To provide a qualitative example of error of the sensitivity matrices, results from the three registration methods for a given subject are shown in Fig. 9. The mean relative error of the sensitivity matrices for all subjects within the ROI are used for quantitative evaluation of the inaccuracy of sensitivity matrices (Fig. 10). The relative errors of sensitivity matrices in ROI vary from less than 20% to more than 300%. For the same landmark system, NP2P and P2P methods have a slight advantage over ICP method. Basic-4 landmark registration, line-fitting registration and full-head landmark registration with NP2P and P2P show an advantage over other registration methods which is consistent with the evaluation result of the surface geometry error.

#214009 - $15.00 USD Received 13 Jun 2014; revised 21 Aug 2014; accepted 25 Sep 2014; published 13 Oct 2014

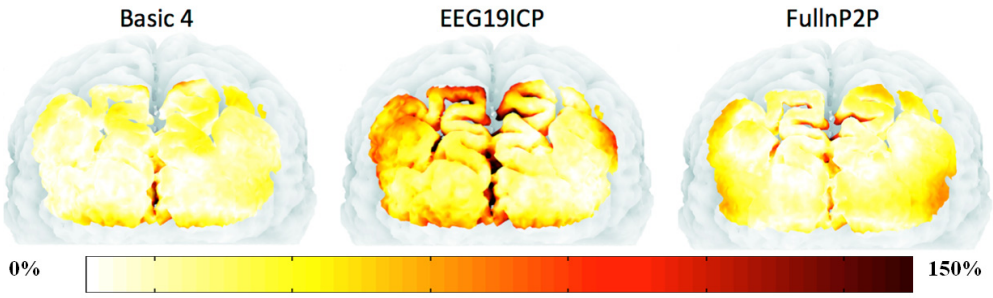

Fig. 9. Example of relative error of sensitivity matrices on the cortex. Note that only the regions with a total sensitivity greater that 1% of the maximum value are shown.

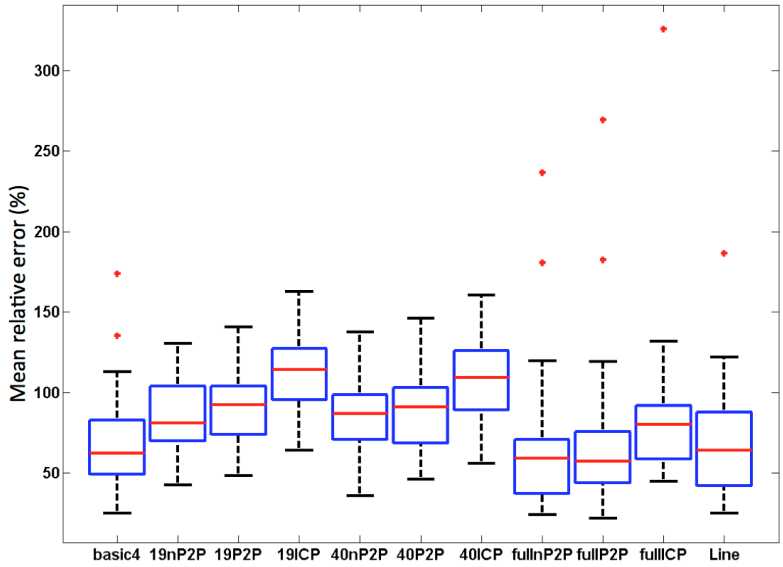

Fig. 10. Mean relative sensitivity error for different registration methods for all 24 subjects. The central (red) lines represent the median, the box plots represent the 25th and 75th percentiles, whereas the whiskers present +/– 2.7 standard deviations. Outliers are presented as red crosses.

In order to evaluate the correlation of these results with the geometric error data, the average mean error (for all 24 subjects) of both parameters (surface error versus sensitivity at the cortex) is plotted for each registration method in Fig. 11. It is seen that based on the average error, across all 24 subjects, there is a strong correlation between surface geometry error and cortex sensitivity error. The basis-4 landmark system is an anomaly, which can be explained by the fact that one of the four landmarks placed over the back of the head is providing a strong fiducial for registration. Ignoring the data from the basic 4 landmark system the calculate R^2 value is 0.97, indicating that the surface geometry error can be used as a surrogate for approximating the error for sensitivity at the cortex surface.

#214009 - $15.00 USD Received 13 Jun 2014; revised 21 Aug 2014; accepted 25 Sep 2014; published 13 Oct 2014

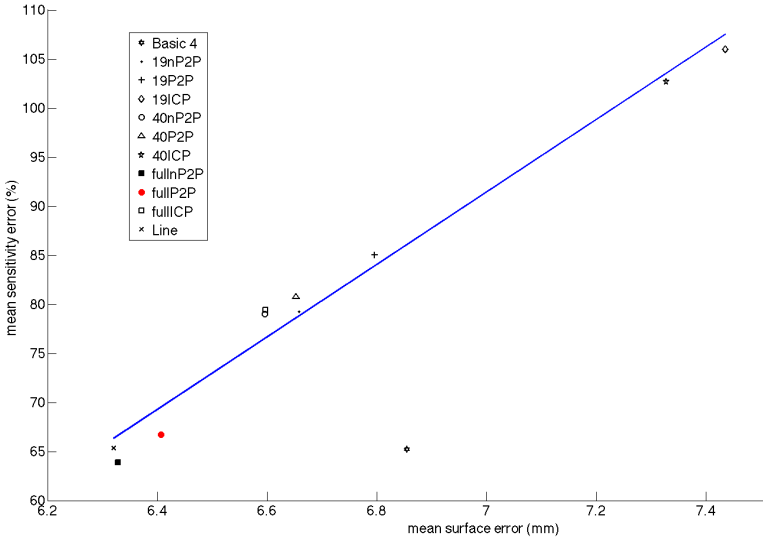

Fig. 11. Mean relative sensitivity error 24 subjects versus mean surface error. Note that the 4 basic landmark data is not considered for the R^2 value or the best fit line.

Evaluation of simulated focal activation result from all 24 subjects is based on the accuracy of recovered activation region. As an example, simulated activations of a given subject and the recovery result based on three registered atlas models as well as the subject specific model are shown in Fig. 12. Quantitative evaluations of the results from both the subject specific and registered atlas models are shown in Fig. 13. The most striking result is that although it has been shown that geometric surface error (and hence) sensitivity error (light propagation error) can be substantial depending on different types of registration algorithms, no single algorithm is providing errors greater than 4.5 mm in location error. This is perhaps expected as in most functional DOT imaging experiments, we are concerned with dynamic (often referred to temporal or difference) imaging, whereby rather than recovering an absolute image of optical properties, we are only concerned with recovery of changes with respect to a baseline and this type of image recovery has shown to be less prone to geometric and model errors as compared to static (absolute) imaging [14, 47, 48]. The relative overlay depends (as expected) on the threshold value and is closer to the expected 100% using the 70% threshold. Nonetheless, all atlas based models overestimate the volume of the recovered activation ranging from 120% to ~200%. Conversely, the relative overlay is much better with 50% threshold (as expected) at the expense of larger volume being recovered. The recovered contrast for all models is approximately the same with ~16% for 50% threshold and ~18% for 70% threshold.

The subject specific mesh provided the best results with a 1.2 mm average location error and provides the most accurate recovery in terms of volume recover and overlay, regardless of whether 50% or 70% threshold is used. Basic 4 landmark registration, line-fitting registration and full-head landmark registration with NP2P and P2P show the best results using the atlas based models which is consistent with previous results.

#214009 - $15.00 USD Received 13 Jun 2014; revised 21 Aug 2014; accepted 25 Sep 2014; published 13 Oct 2014

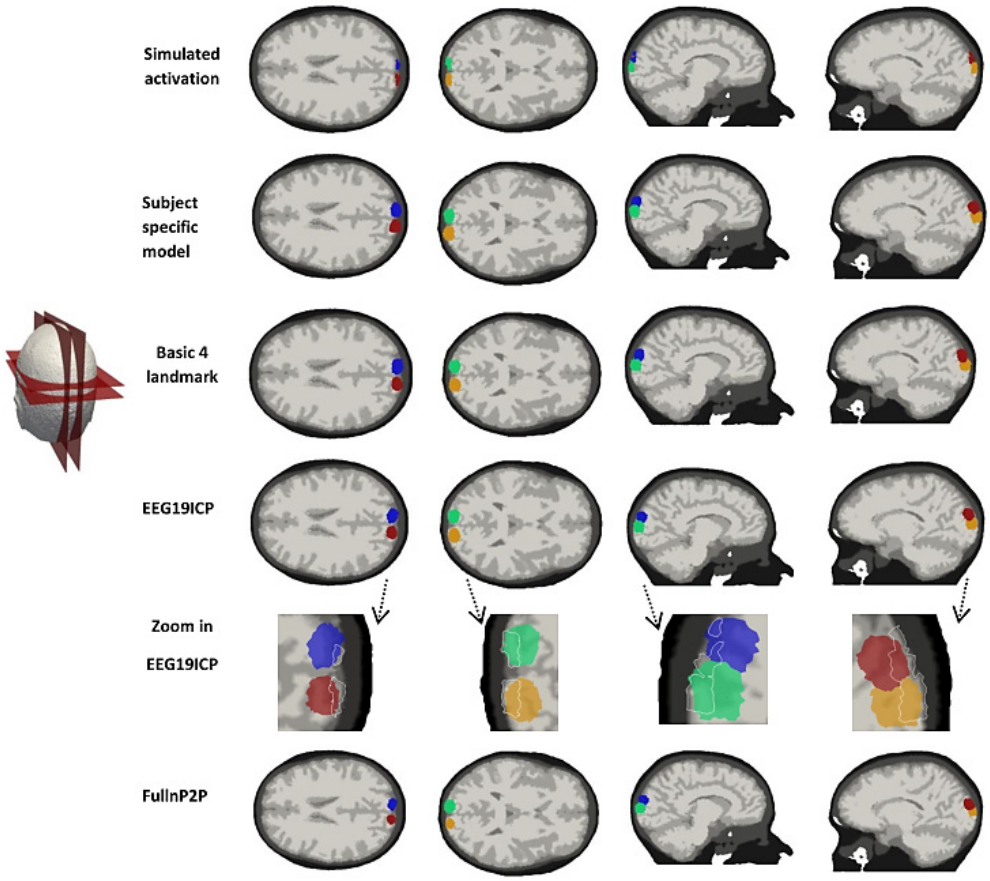

Fig. 12. Example of focal activation recovery result for a single subject based on subject specific model and three registered atlas models. Note that each individual activation is color-coded and represent an individual simulation. White lines in the zoomed in plots represent the simulated activation.

#214009 - $15.00 USD Received 13 Jun 2014; revised 21 Aug 2014; accepted 25 Sep 2014; published 13 Oct 2014

Fig. 13. Evaluation of focal activation recovery for all registration methods across all 24 subjects.

4. Conclusion

In this work, a detailed workflow for the utilisation of atlas based models for image recovery in DOT is demonstrated with strong emphasis on High Density DOT of the visual cortex. In contrast to previously published work, 11 different registration algorithms have been utilised, using 24 different subjects. Additionally, the presented work has concentrated not only on analysing the geometrical match between different registration models, or evaluation of recovered focal activations, but also provides a quantitative evaluation of induced errors in estimated of internal tissue structural distributions and their effect on the accuracy of the light propagation model.

It has been shown that all the registration methods provide recovery results for activations in visual cortex, which are less than 4.5 mm in localisation error. Although the difference in accuracy between different registration methods is not significant, the overall comparison of

#214009 - $15.00 USD Received 13 Jun 2014; revised 21 Aug 2014; accepted 25 Sep 2014; published 13 Oct 2014

accuracy of all the three steps (registration, light propagation model and image recovery) are consistent, which indicates that the accuracy of registration has a direct effect on accuracy of the corresponding sensitivity matrix and hence the corresponding recovery result. Comparing different algorithms, registration methods with NP2P and P2P optimization algorithms demonstrate a slight advantage over ICP optimization algorithms using the same landmark system on geometry errors, accuracy of the sensitivity matrices and the focal recovery. This is because point to point optimization algorithms aim to register corresponding landmark pairs specifically instead of closest landmark pair which is more accurate. Basic-4 landmark registration, line-fitting registration and full-head landmark registration with NP2P and P2P show an advantage over other registration methods. The improved accuracy of the full-head landmark registration is primarily due to the high- density of landmark sets utilised.

For basic-4 landmark registration, since one of the four landmarks are extracted from inion which is on the surface of scalp directly above vision cortex registration method has shown better accuracy in this study, which is also true for the line-fitting algorithm. These may not be the case if the study was based on other regions of the brain, for example the motor cortex, for which other landmark systems may provide a better accuracy.

Focal activation recovery results from the 50% and 70% thresholds have almost the same location error, with basic-4 landmark, line-fitting and full-head landmark registration using NP2P and P2P demonstrating better results. All models have a similar average contrast, though it is slightly higher for the 70% threshold. All proposed rigid registration methods show a similar accuracy on the recovery of activated area in visual cortex. However, with more landmarks needed for the registration, the landmark extraction and computational process become more complex and iterative process tends to increase the calculation time. For non-iterative processes, the computation time is usually a few seconds, but for an iterative process, it can be up to few minutes. Considering these two aspects, for recovery of focal activations in visual cortex, a registration method based on basic-4 landmark system is the most efficient method among the studied algorithms for atlas based DOT. However, other landmark systems may provide better accuracy when considering regions other than the visual cortex.

Acknowledgments

This work has been funded by the National Institutes of Health (NIH) Grant R01EB009233-2 RO1-CA132750 and Autism Speaks Meixner Translational Postdoctoral Fellowship 7962.

#214009 - $15.00 USD Received 13 Jun 2014; revised 21 Aug 2014; accepted 25 Sep 2014; published 13 Oct 2014